RSC Advances

ROYAL SOCIETY OF CHEMISTRY

www.rsc.org/advances

Facile synthesis of hierarchical worm-like MoS_2 structures assembled with nanosheets as anode for lithium ion batteries

Hui-Yuan Wang, Bang-Yong Wang, Dong Wang, Lun Lu, Jin-Guo Wang, Qi-Chuan Jiang*

Key Laboratory of Automobile Materials of Ministry of Education & School of Materials Science and Engineering, Jilin University, Changchun 130025, China

Abstract: Hierarchical worm-like MoS_2 structures directionally assembled with nanosheets are successfully synthesized via a simple hydrothermal route using potassium sodium tartrate as a structure-directing agent. The possible growth mechanism of worm-like MoS_2 structures is proposed through controlling hydrothermal temperature, time and the amount of potassium sodium tartrate. The results indicate that potassium sodium tartrate plays important roles in formation of worm-like structures. The unique hierarchical structures as an anode for lithium-ion batteries display high specific capacity of 845 mAh g^{-1} after 50 cycles at 100 mA g^{-1} and good cyclic stability of 698 mAh g^{-1} even at high rate of 500 mA g^{-1} after 100 cycles. The excellent electrochemical performance can be attributed to the hierarchical surface, sufficient void space between neighboring nanosheets and unique worm-like structures. Besides, this work also provides a simple strategy to design and construct other structural materials, such as layered metal sulfides and oxides.

* Corresponding author: Professor Jin-Guo Wang (J.-G. Wang)
Tel/Fax: +86 431 8509 4699. E–mail: wanghuiyuan@jlu.edu.cn; jgwang@jlu.edu.cn (J.-G. Wang);

1. Introduction

The growing requirement for high-power and high-capacity lithium ion batteries (LIBs) in the emerging technologies (e.g., electric vehicles, hybrid electric vehicles and grid storage) has prompted tremendous research efforts towards developing high-performance electrode materials.[1] During the past decade, molybdenum disulfide (MoS_2) has attracted considerable attention as an anode material because of its layered structure analogous to graphene.[2-12] The S-Mo-S sandwich layers are stacked together by weak van der Waals interactions, which facilitate the intercalation/deintercalation of lithium ions without initiating large volume expansion. However, just like graphene, MoS_2 nanosheets are liable to aggregate in practical application, which will result in the decrease of exposed surface area and the loss of active sites, leading to fast capacity fading.

To address the above problems, one strategy is to design growth of MoS_2 nanosheets on carbonaceous medium, such as CNTs,[12-15] carbon nanofibers,[16] polyaniline nanowires,[10] carbon spheres,[17-19] graphene foam[9] and graphene nanosheets.[4,8] The carbonaceous medium can not only preserve the good dispersity of individual nanosheet and suppress their aggregation during charge–discharge cycles, but also increase the electronic conductivity of the electrodes. Another strategy is to construct hierarchical structures with nanosheets to maintain good structural integration.[2,9,17,20-22] Such hierarchical structures synergistically combine the merits of both microstructures and nanostructures, which can not only provide fast lithium-ion insertion/extraction, but also avoid effectively the aggregation of nano-building blocks, thus demonstrating improved cyclic stability and rate capacity. Recently, some hierarchical MoS_2 micro/nano-structures, such as tubular architectures,[2] microboxes,[3] nanowalls[5] and hollow nanoparticles[6] have been reported as an anode material for LIBs and deliver good electrochemical performance. Theoretically, hierarchical layered structures can be obtained through directional self-assembly of nanosheets. For example, Liu and co-workers[23] reported hierarchical worm-like $Co_{1-x}S$ (x=0.75) microtubes assembled by hexagonal nanoplates via a one-pot hydrothermal method with the co-assistance of CTAB and ethylenediamine, which exhibited good electrochemical and magnetic properties. More recently, Xu and co-workers[24] reported a solvothermal method for the synthesis of

worm-like MoS_2 structures constructed by nanosheets in the solution of octylamine, ethanol and water for the first time. The worm-like structures exhibit good electrochemical properties as anode materials for sodium ion batteries. Obviously, the preparation of such hierarchical structures needs proper structure-directing agents, which assist directional interconnection or assembly of nanosheets.[25] However, to the best of our knowledge, no report has been made on the synthesis of MoS_2 with hierarchical worm-like morphologies as anodes for LIBs.

Herein, we report a simple hydrothermal method to prepare hierarchical worm-like MoS_2 structures directionally assembled by nanosheets with the assistance of potassium sodium tartrate. According to the literature,[26-28] potassium sodium tartrate can effectively induce the synthesis of nanostructure materials. The morphologies and formation of as-prepared products can be well controlled by adjusting hydrothermal time, temperature and the amount of potassium sodium tartrate. When evaluated as an anode material for LIBs, the worm-like MoS_2 show high specific capacity and excellent cyclic stability, exhibiting great practical prospect.

2. Experimental Section

2.1 Material preparation

Analytical-grade $Na_2MoO_4 \cdot 2H_2O$, NH_2CSNH_2 and potassium sodium tartrate ($C_4H_4O_6KNa \cdot 4H_2O$) were used as received without further purification. In a typical procedure, 0.2 g Na_2MoO_4, 0.4 g NH_2CSNH_2 and 1 mmol $C_4H_4O_6KNa$ were dissolved in 20 ml deionized (DI) water to form a transparent solution. Then the resulting mixture was transferred into a Teflon-lined stainless steel autoclave and heated to 200 ^oC for 24 h. After cooling to ambient temperature, the black precipitate was collected by centrifuging and washed with DI water and ethanol, respectively, and finally dried in an electric oven at 60 ^oC for 12 h. To investigate the formation process of hierarchical worm-like MoS_2 structures, intermediate products were collected at the hydrothermal time of 7, 8 and 12 h, respectively. Meanwhile, controlled experiments were also conducted at different hydrothermal temperatures (180 and 220 ^oC) and with different amounts of tartrate (0, 0.5 and 2 mmol).

2.2 Material characterization

The crystal structures of the samples were characterized by X-ray powder diffraction (XRD, Rigaku-D/Max 2500PC/Japan, using Cu Kα radiation, λ = 1.5406 Å). The morphologies of the samples were investigated using field emission scanning electron microscopy (FESEM, JSM-6700F, Japan) and transmission electron microscopy (TEM, JEM-2100F, 200 kV). X-ray photo-electron spectrometry (XPS) with an ESCALAB250 analyzer was employed to evaluate the chemical status of the samples. The nitrogen adsorption and desorption isotherms were collected using an ASAP 2020 surface area and porosity analyzer. The pore size distribution was calculated using the Barrett–Joyner–Halenda (BJH) methods.

2.3 Electrochemical measurements

The products were mixed with acetylene black and sodium carboxymethyl cellulose (CMC) at a weight ratio of 70: 20: 10 to form proper slurry. The slurry was uniformly pasted on Cu foil and such prepared electrode sheets were dried at 120 ^{o}C for 12 h in a vacuum oven. The CR2025-type half-coin cells were assembled in an argon-filled glove box with the contents of H_2O and O_2 below 1 ppm. Metallic lithium foil was used as the counter and reference electrode. The electrolyte consists of a solution of 1 M $LiPF_6$ in mixture of ethylene carbonate (EC), ethyl methyl carbonate (EMC) and dimethyl carbonate (DMC) with a volume ratio of 1: 1: 1. Charge-discharge performance was evaluated by a LAND CT2001A battery instrument at a constant current density in the voltage range of 0.01–3.0 V at room temperature. Cyclic voltammetry (CV) tests were performed between 0.01 and 3.0 V at a scan rate of 0.1 mV s^{-1} on a CHI650D electrochemical workstation.

3. Results and discussion

The morphology and structure of the as-synthesized products were characterized by FESEM and TEM techniques, as shown in Fig. 1. The low-magnification FESEM view (Fig.1a) shows that as-prepared products consist of uniform one-dimensional worm-like structures with the average diameters of about 250 nm. The magnified FESEM image (Fig. 1b) clearly reveals that the worm-like structures are directionally constructed by nanosheets with the average thickness of 12 nm. Fig. 1c shows TEM observation of the products, which further confirms the structural feature. The nanosheets densely

stacked together to form one-dimensional hierarchical structures. In addition, the relatively large exposed surface and void space between nanosheets could also been observed. The high-resolution TEM image shows the edge view of some nanosheets with clear lattice fringes (Fig. 1d). The interplanar spacing is measured to be about 0.64 nm, well corresponding to (002) plane of hexagonal-structured MoS_2. The selected area electron diffraction (SAED) pattern exhibits a serials of diffraction rings, demonstrating the polycrystalline nature of MoS_2 (the inset of Fig. 1d). It is worth noting that Mitra et al.[5] reported that ultrasonic treatment can lead to the separation of MoS_2 flakes, causing that the agglomerated cauliflower morphology is invisible in TEM images. Interestingly, however, the intact morphology of MoS_2 structures self-assembled here can be still observed under TEM analysis, indicating high binding strength between nanosheets.

To get more insight into the morphological evolution of hierarchical worm-like MoS_2 structures, a serials of time-dependent experiments were carried out in our work and the intermediated products were collected for FESEM analysis. To our surprise, even though the hydrothermal time reached 6 h, no precipitate was yet obtained and the color of the solution only changed from colorless to red brown. When the reaction time increased to 7 h, black precipitates began to turn up, indicating that the nucleation rate of MoS_2 crystals is very slow in the reaction system. The slow nucleation rate facilitates the controllable formation of regular MoS_2 nanostructures. Fig. 2a-c shows FESEM images of the products collected after 7, 8 and 12 h of reaction. In the initial stage, the products consist of nanoparticles with diameters of about 50 nm (Fig. 2a). It can be also clearly seen that these nanoparticles show orderly arrangement according to a certain orientation rather than in a random or disordered distribution. With the reaction time prolonging, on the one hand, the nanoparticles will continue to nucleate at both ends of ordered nanoparticle arrays along axis direction; on the another hand, the nanoparticles will gradually grow to nanosheets along radial direction (Fig. 2b-c). Finally, worm-like MoS_2 structures constructed by nanosheets are obtained (Fig. 1a).

Compared with other reported synthesis methods, the successful preparation of hierarchical worm-like MoS_2 structures is mainly attributed to the addition of $C_4H_4O_6KNa$. It is worth mentioning that the

additive amounts of $C_4H_4O_6KNa$ have a great effect on the morphology of final products (Fig. 2d-f). Without the addition of $C_4H_4O_6KNa$, the products exhibit bulk structures with sizes of several micrometers, which are randomly agglomerated by nanosheets (Fig. 2d). When slight $C_4H_4O_6KNa$ is used (0.5 mmol), the morphology with regular agglomerated nanosheets is observed (Fig. 2e). When a proper amount is used (1 mmol), hierarchical worm-like structures directionally assembled by nanosheets are obtained (Fig. 1a). Therefore, according to the experimental results, the possible growth process of hierarchical worm-like MoS_2 structures is proposed. In the reaction system, tartrate ions ($C_4H_4O_6^{2-}$) firstly conjugate with Mo-containing ions to form the soluble complex. As the hydrothermal reaction continues, thiourea is hydrolyzed to release S^{2-} ions, which will slowly react with Mo^{4+} to form MoS_2 nanoparticles. Meanwhile, $C_4H_4O_6^{2-}$ ions may be absorbed on the surface of MoS_2 nanoparticles and assist ordered array of primary nanoparticles and prevent their aggregation. With the reaction time increasing, MoS_2 nanoparticles gradually grow to form nanosheets along (002) plane. Consequently, hierarchical worm-like MoS_2 structures are constructed by oriented function of $C_4H_4O_6^{2-}$ ions. Nevertheless, excess $C_4H_4O_6KNa$ (2 mmol) will result in the synthesis of agglomerates of nanoparticles (Fig. 2f). The reason may be that excess $C_4H_4O_6^{2-}$ is attached on the surface of nanoparticles and inhibits their growth during the reaction process. In addition, the influence of the reaction temperature on the morphology of the products was also studied. From FESEM analysis (Fig. 3), distinct morphological difference can be observed, indicating the construction of worm-like structures is also controlled by thermodynamics and kinetics of the reaction. Therefore, the possible formation process of hierarchical worm-like MoS_2 structures can be described as shown in Scheme 1. Such structures are beneficial for accommodating the volume change during the Li^+ intercalation because of enough void space between neighboring nanosheets and providing more exposed active sites for lithium storage. As a result, excellent electrochemical performance can be obtained from hierarchical worm-like MoS_2 structures.

The X-ray powder diffraction measurement was used to investigate the crystal structure and phase purity of the samples. Fig. 4a (top) shows XRD pattern of hierarchical worm-like MoS_2. All of the diffraction peaks can be well indexed to hexagonal MoS_2 (JCPDS no. 37-1492), indicating high purity

of the sample.[29] The XRD pattern of the product prepared without the addition of $C_4H_4O_6KNa$ (denoted as bulk MoS_2, FESEM image seen in Fig. 2d) is also shown and similar to that of worm-like MoS_2 (Fig. 4a, bottom). The X-ray photoelectron spectroscopy was conducted to analyze the chemical states of Mo and S in the worm-like MoS_2 structures. The binding energies of Mo $3d_{5/2}$ and Mo $3d_{3/2}$ are found to be at 227.96 and 231.24 eV, respectively, which are attributed to Mo^{4+} in MoS_2 (Fig. 4b). A small S 2s peak is also found at 225 eV. The peaks centered at 160.70 and 161.96 eV are assigned to the S $2p_{3/2}$ and S $2p_{1/2}$ peaks of S^{2-} in MoS_2 (Fig. 4c).[30] The specific surface area and pore size distribution of worm-like MoS_2 structures were also characterized by nitrogen adsorption–desorption isothermal measurement, as shown in Fig. 4d. The isotherm profile of the sample can be categorized as a type IV curve, implying the presence of mesoporous structures.[18] The specific surface area is measured to be about 13 m^2 g^{-1} by the Brunauer–Emmett–Teller (BET) method. Moreover, the pore size distribution is calculated by Barret–Joyner–Halenda (BJH) analysis (inset of Fig. 4d). The sharp peak centered at 3.5 nm is attributed to mesoporous channels deriving from ordered stack of MoS_2 nanosheets.[2,18] Besides, nitrogen adsorption–desorption isotherm of bulk MoS_2 prepared without the addition of $C_4H_4O_6KNa$ was also investigated (Fig. S1). Their BET surface area is calculated to be only 0.99 m^2 g^{-1}, greatly lower than that of worm-like MoS_2 structures. The result further demonstrates that $C_4H_4O_6KNa$ can effectively hinder random agglomeration of nanosheets and assist the directional assembly of nanosheets, resulting in large surface area, which is beneficial for energy storage.

The electrochemical performance of as-prepared worm-like MoS_2 was investigated as an anode material for LIBs via cyclic voltammetry (CV) and galvanostatic discharge–charge measurements, as shown in Fig. 5. Fig. 5a shows the first three cyclic voltammograms of hierarchical worm-like MoS_2 at a scan rate of 0.1 mV s^{-1} between 0.01 and 3.0 V. It is clearly seen that the curve of the first cycle in the cathodic scan is substantially different from the subsequent ones. In the first cycle, a small peak at 1.1 V in the cathodic scan is ascribed to the intercalation of Li^+ into MoS_2 layers, accompanying the formation of Li_xMoS_2. The peak located at around 0.5 V is mainly assigned to the conversion reaction process which involves the decomposition of Li_xMoS_2 into Mo metal particles embedded into a Li_2S matrix.[9,30-

[33] In the anodic process, two defined oxidation peaks are observed at around 1.75 and 2.25 V. The explanations given in the literature for the origin of the two peaks are debatable. In general, the small peak at 1.75 V is due to the partial oxidation of Mo to form MoS_2 and the dominant oxidation peak at 2.25 V may be attributed to the formation of sulfur by oxidation of Li_2S.[9,30-33] As a result, after the first cycle, the electrode is mainly composed of Mo, S and less MoS_2 instead of the initial MoS_2. In the second cycle, the locations of cathodic peaks are transferred to 1.33 and 1.92 V, probably corresponding to the multistep reaction of S with lithium while the anodic process almost does not change. From the second cycle on, the CV curves are overlapped perfectly, implying excellent reversibility of the electrochemical reactions.

Fig. 5b shows the discharge-charge voltage profiles of hierarchical worm-like MoS_2 at a current density of 100 mA g^{-1} in a voltage range of 0.01–3.0 V. The initial discharge and charge capacities are 812 and 693 mAh g^{-1}, respectively, corresponding to the initial Coulombic efficiency of 85.3 %. Such a high initial Coulombic efficiency is attributed to the unique hierarchical structures, which facilitate the insertion/extraction of Li^+ ions. From the second cycle onwards, the Coulombic efficiency rapidly increases to > 97 %. The cyclic performance of hierarchical worm-like MoS_2 tested in the current density of 100 mAh g^{-1} is shown in Fig. 5c. A stable capacity of 845 mAh g^{-1} can be maintained after 50 cycles with a high Coulombic efficiency of around 99 %. It is interesting to note that the phenomenon of the gradual increased capacity probably results from a gradual activation process of the electrodes as well as the reversible formation of a polymeric gel-like film on the electrode.[28] For comparison, the cyclic performance of bulk MoS_2 is also included in Fig. 5c. Obviously, bulk MoS_2 exhibits much faster capacity fading and only a capacity of around 588 mAh g^{-1} is retained after 50 cycles. Furthermore, to evaluate the rate capacities, hierarchical worm-like MoS_2 and bulk MoS_2 were also investigated at various current densities from 100 to 1000 mA g^{-1}, as shown in Fig. 5d. Remarkably, hierarchical worm-like MoS_2 exhibit superior rate capacities than bulk MoS_2. The reversible discharge capacities at 100, 200, 500 and 1000 mA g^{-1} for hierarchical worm-like MoS_2 are 826, 753, 707 and 677 mAh g^{-1} with 96–99 % Coulombic efficiency, respectively, while 638, 574, 477 and 397 mAh g^{-1} for bulk MoS_2.

Moreover, as the current rate returns back to 100 mA g^{-1}, a high capacity of 882 mAh g^{-1} can be still recovered for hierarchical worm-like MoS_2, much higher than that of bulk MoS_2 (584 mAh g^{-1}). In the worm-like MoS_2 the overall capacity and rate capability are much higher than that of bulk MoS_2. This is a direct result of the electrode structure, where worm-like nanostructure reduces the solid-state diffusion distances and promotes more facile lithiation/delithiation at a given current density.[34]

In addition, to probe the electrochemical properties of worm-like MoS_2 structures at large current density, the electrochemical test was performed at a current density of 500 mA g^{-1}, as shown in Fig. 6. Noticeably, the high discharge capacity can be still maintained at 698 mAh g^{-1} after 100 cycles with a Coulombic efficiency of around 97 %. Such good cyclic performance at high current rate is also higher compared to that of some reported MoS_2-C composites in the literature.[17,18,35] C@MoS_2 quasi-hollow microspheres prepared utilizing monodisperse SPS microspheres as both template and carbon source delivered a specific capacity of 652 mAh g^{-1} at 100 mA g^{-1} after 100 cycles.[17] C-MoS_2 nanorods synthesized using MoO_3 nanorods as the precursor via chemical vapor deposition of sulfidation process and carbon layer exhibited a 621 mAh g^{-1} at 200 mA g^{-1} after 80 cycles.[35] Besides, the morphology of the electrode after 100 cycles was also characterized by FESEM technique, as shown in Fig. S2. The worm-like structure can still be observed after 100 cycles, indicating attractive structural stability. We believe that the improved lithium storage properties of as-prepared MoS_2 are probably due to the unique worm-like structures. Specifically, the large surface area provided by directionally assembled nanosheets endows hierarchical structures with more exposed reactive sites and large electrode-electrolyte contact area, thus leading to high specific capacities. Furthermore, enough free space between neighboring nanosheets not only can facilitate lithium ions diffusion but also release the mechanical stress deriving from volume change during the discharge-charge process, resulting in excellent cyclic stability.

4. Conclusions

In summary, we have designed a simple hydrothermal route to synthesize hierarchical worm-like MoS_2 structures directionally constructed by nanosheets with the assistance of potassium sodium tartrate. It was clearly found that hydrothermal time, temperature and the amount of potassium sodium tartrate

could sensitively affect the formation of the products. When evaluated as an anode material for LIBs, a higher specific capacity of 845 mAh g^{-1} after 50 cycles at 100 mA g^{-1} were achieved compared to bulk MoS_2. Even at 500 mA g^{-1}, the reversible capacity still could be kept at 698 mAh g^{-1} after 100 cycles. The excellent electrochemical performance of worm-like MoS_2 makes them a promising anode material for LIBs. In addition, we believe that the simple strategy can be used to design other structural materials because of the flexibility of potassium sodium tartrate.

Acknowledgment

The authors acknowledge financial support from The Fundamental Research Funds for the Central Universities (JCKY-QKJC02), The Foundation of Jilin University for Distinguished Young Scholars and Project 985-Materials Science and Engineering of Jilin University.

References

1 M. Armand and J. M. Tarascon, *Nature*, 2008, **451**, 652.

2 P. P. Wang, H. Y. Sun, Y. J. Ji, W. H. Li and X. Wang, *Adv. Mater.*, 2014, **26**, 964.

3 L. Zhang, H. B. Wu, Y. Yan, X. Wang and X. W. Lou, *Energy Environ. Sci.*, 2014, **7**, 3302.

4 Y. T. Lu, X. Y. Yao, J. Y. Yin, G. Peng, P. Cui and X. X. Xu, *RSC Adv.*, 2015, **5**, 7938.

5 U. K. Sen and S. Mitra, *ACS Appl. Mater. Interfaces*, 2013, **5**, 1240.

6 M. Wang, G. Li, H. Xu, Y. Qian and J. Yang, *ACS Appl. Mater. Interfaces*, 2013, **5**, 1003.

7 G. Du, Z. Guo, S. Wang, R. Zeng, Z. Chen and H. Liu, *Chem. Commun.*, 2010, **46**, 1106.

8 W. D. Qiu, J. Q. Jiao, J. Xia, H. M. Zhong and L. P. Chen, *RSC Adv.*, 2014, **4**, 50529.

9 J. Wang, J. L. Liu, D. L. Chao, J. X. Yan, J. Y. Lin and Z. X. Shen, *Adv. Mater.*, 2014, **26**, 7162.

10 L. C. Yang, S. N. Wang, J. J. Mao, J. W. Deng, Q. S. Gao, Y. Tang and O. G. Schmidt, *Adv. Mater.*, 2013, **25**, 1180.

11 J. Xiao, D. Choi, L. Cosimbescu, P. Koech, J. Liu and J. P. Lemmon, *Chem. Mater.*, 2010, **22**, 4522.

12 D. Y. Ren, H. Jiang, Y. J. Hu, L. Zhang and C. Z. Li, *RSC Adv.*, 2014, **4**, 40368.

13 S. J. Ding, J. S. Chen and X. W. (David) Lou, *Chem. Eur. J.*, 2011, **17**, 13142.

14 Y. M. Shi, Y. Wang, J. I. Wong, A. Y. S. Tan, C. L. Hsu, L. J. Li, Y. C. Lu and H. Y. Yang, *Sci. Rep.,* 2013, **3**, 2169.

15 C. X. Lu, W. W. Liu, H. Li and B. K. Tay, *Chem. Commun.*, 2014, **50**, 3338.

16 F. Zhou, S. Xin, H. W. Liang, L. T. Song and S. H. Yu, *Angew. Chem. Int. Ed.*, 2014, **53**, 11552.

17 Z. M. Wan, J. Shao, J. J. Yun, H. U. Zheng, T. Gao, M. Shen, Q. T. Qu and H. H. Zheng, *Small*, 2014, **10**, 4975.

18 S. J. Ding, D. Y. Zhang, J. S. Chen and X. W. Lou, *Nanoscale*, 2012, **4**, 95.

19 L. Zhang and X. W. (David) Lou, *Chem. Eur. J.*, 2014, **20**, 5219.

20 L. Hu, H. Zhong, X. R. Zheng, Y. M. Huang, P. Zhang and Q. W. Chen, *Sci. Rep.*, 2012, **2**, 986.

21 J. Y. Xiang, J. P. Tu, L. Zhang, Y. Zhou, X. L. Wang and S. J. Shi, *J. Power Sources*, 2010, **195**, 313.

22 S. L. Jin, H. G. Deng, D. H. Long, X. J. Liu, L. Zhan, X. Y. Liang, W. M. Qiao and L. C. Ling, *J. Power Sources*, 2011, **196**, 3887.

23 B. Liu, S. Wei, Y. Xing, D. Liu, Z. Shi, X. C. Liu, X. J. Sun, S. Y. Hou and Z. M. Su, *Chem. Eur. J.*, 2010, **16**, 6625.

24 M. W. Xu, F. L. Yi, Y. B. Niu, J. L. Xie, J. K. Hou, S. G. Liu, W. H. Hu, Y. T. Li and C. M. Li, *J. Mater. Chem. A*, 2015, **3**, 9932.

25 Z. L. Zhang, Q. Q. Tan, Y. F. Chen, J. Yang and F. B. Su, *J. Mater. Chem. A*, 2014, **2**, 5041.

26 G. Y. Li, Y. H. Ni, J. M. Hong and K. M. Liao, *CrystEngComm.*, 2008, **10**, 1681.

27 Z. G. An, S. L. Pan and J. J. Zhang, *J. Phys. Chem. C*, 2009, **113**, 2715.

28 B. Y. Wang, H. Y. Wang, Y. L. Ma, X. H. Zhao, W. Qi and Q. C. Jiang, *J. Power Sources*, 2015, **281**, 341.

29 X. Xu, Z. Y. Fan, S. J. Ding, D. M. Yu and Y. P. Du, *Nanoscale*, 2014, **6**, 5245.

30 L. R. Hu, Y. M. Ren, H. X. Yang and Q. Xu, *ACS Appl. Mater. Interfaces*, 2014, **6**, 14644.

31 K. Chang and W. X. Chen, *ACS NANO*, 2011, **5**, 4720.

32 U. K. Sen, P. Johari, S. Basu, C. Nayakc and S. Mitra, *Nanoscale*, 2014, **6**, 10243.

33 Y. Hou, J. Y. Li, Z. H. Wen, S. M. Cui, C. Yuan and J. H. Chen, *Nano Energy*, 2014, **8**, 157.

34 Z. W. Xu, H. L. Wang, Z. Li, A. Kohandehghan, J. Ding, J. Chen, K. Cui and D. Mitlin, *J. Phys. Chem. C*, 2014, **118**, 18387.

35 C. F. Zhang, H. B. Wu, Z. P. Guo and X. W. Lou, *Electrochem. Commun.*, 2012, **20**, 7.

Figure captions:

Figure 1. (a, b) FESEM and (c) TEM images of worm-like MoS_2 structures, (d) the high-resolution TEM image, inset of (d): corresponding SAED pattern.

Figure 2. FESEM images of the products synthesized with 1 mmol $C_4H_4O_6KNa$ at 200 ^oC at different hydrothermal time: (a) 7 h, (b) 8 h and (c) 12 h, and FESEM images of the products synthesized for 24 h at 200 ^oC with the different amounts of $C_4H_4O_6KNa$: (d) 0 mmol, (e) 0.5 mmol and (f) 2 mmol.

Figure 3. FESEM images of the products synthesized for 24 h with 1 mmol $C_4H_4O_6KNa$ at different hydrothermal temperature: (a) 180 ^oC and (b) 220 ^oC..

Figure 4. (a) XRD patterns of hierarchical worm-like MoS_2 and bulk MoS_2, high resolution XPS spectra of (b) Mo 3d and (c) S 2p of hierarchical worm-like MoS_2 structures, and (d) N_2 adsorption/desorption isotherms of hierarchical worm-like MoS_2 structures with corresponding pore-size distribution plots (inset).

Figure 5. (a) The cyclic voltammograms of worm-like MoS_2 at a scan rate of 0.1 mV s^{-1}, (b) discharge-charge profiles of worm-like MoS_2 at 100 mA g^{-1}, (c) cyclic performance of worm-like MoS_2 and bulk MoS_2, Coulombic efficiency of worm-like MoS_2 at 100 mA g^{-1}, (d) rate performance of two electrodes at various current densities in the range of 100-1000 mA g^{-1}.

Figure 6. Cyclic performance of worm-like MoS_2 at the current density of 500 mA g^{-1}.

Scheme 1. Schematic illustration of the formation of hierarchical worm-like MoS_2 structures.

Figure 1

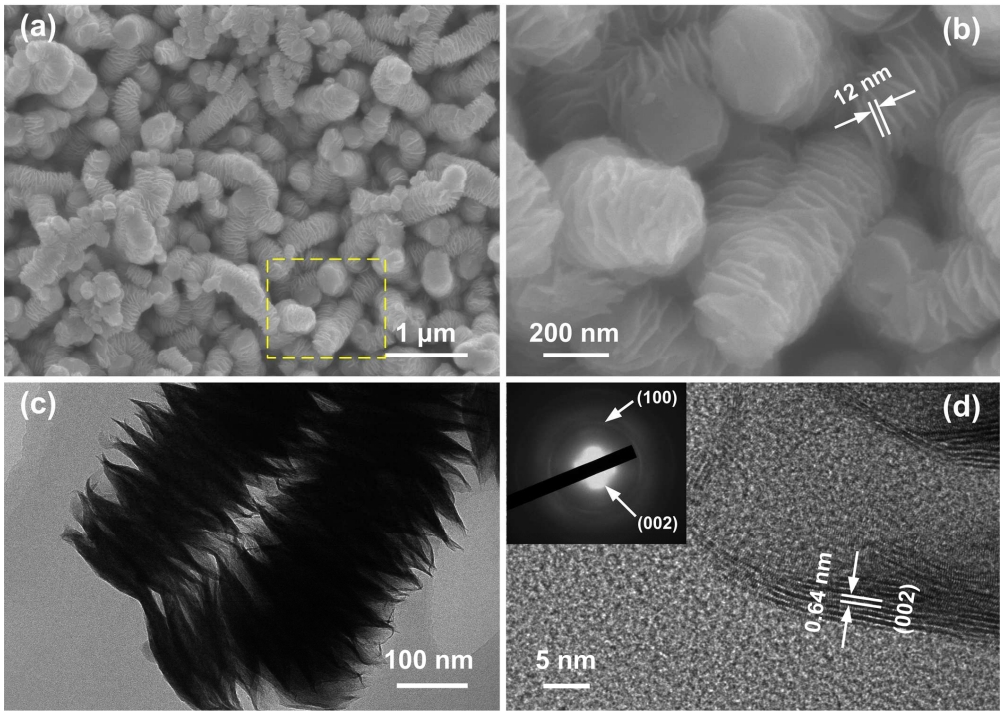

Figure 2

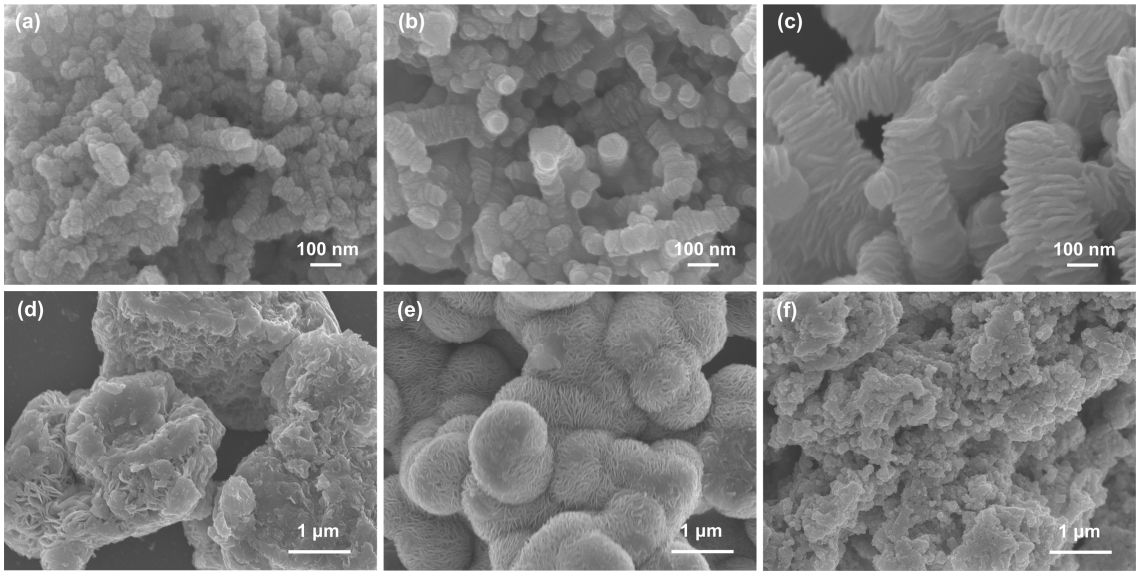

Figure 3

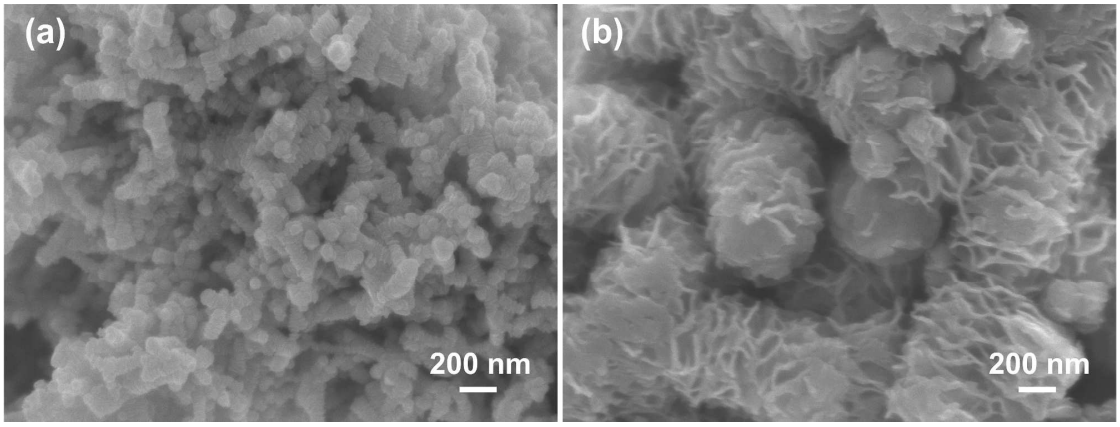

Scheme 1

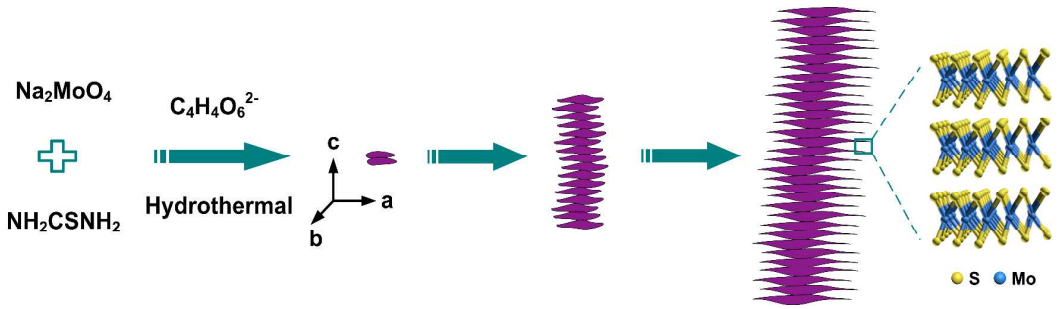

Figure 4

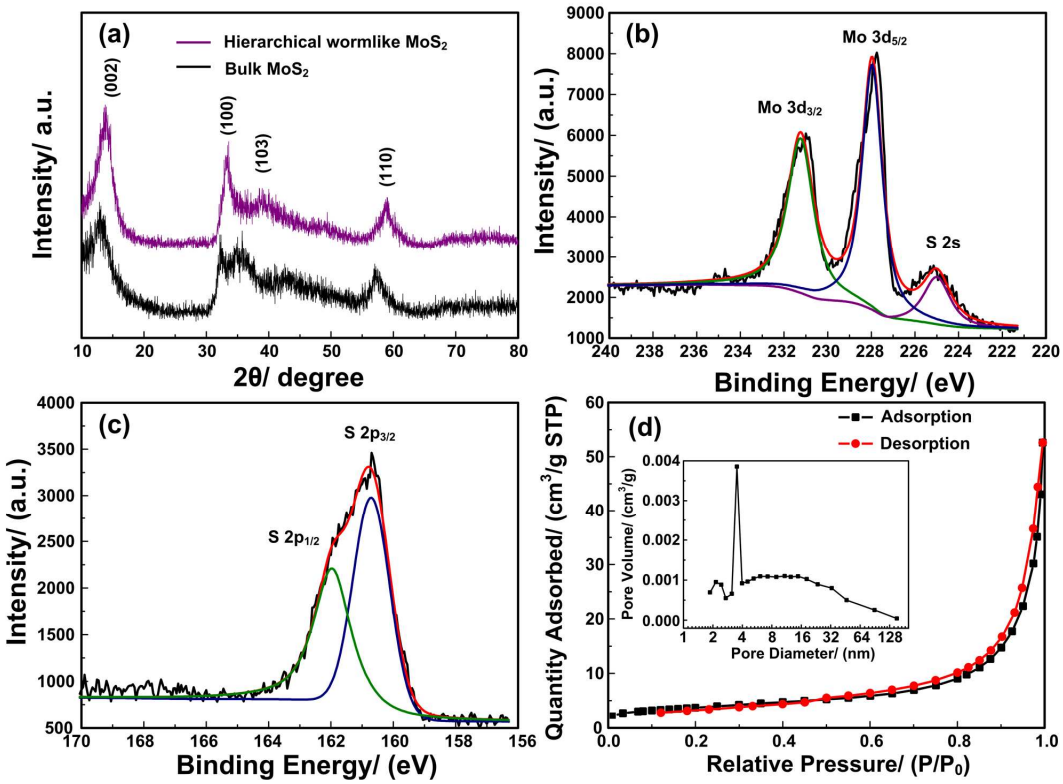

Figure 5

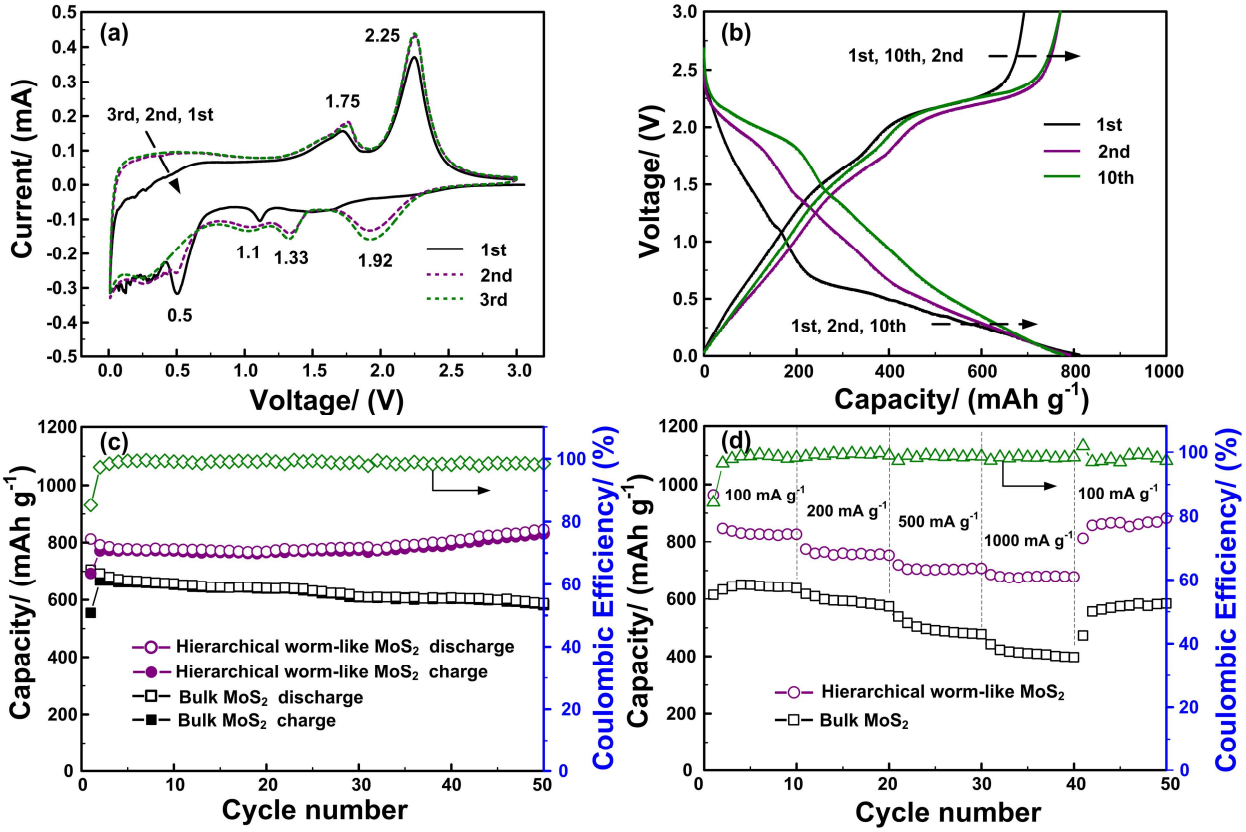

Figure 6